Modelling of capillary water absorption in sound and cracked concrete using a dual-lattice approach
Computational aspects

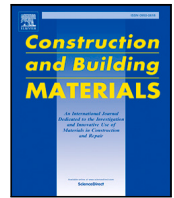Singla, Anmol; Šavija, Branko ; Sluys, Lambertus J.; Romero Rodriguez, C.

Important note
To cite this publication, please use the final published version (if applicable).
Please check the document version above.

Modelling of capillary water absorption in sound and cracked concrete using a dual-lattice approach: Computational aspects

Anmol Singla, Branko Šavija, Lambertus J. Sluys, C. Romero Rodríguez *

Department of 3MD, Faculty of Civil Engineering and Geosciences, Delft University of Technology, Stevinweg 1, 2628CN Delft, The Netherlands

ARTICLE INFO

ABSTRACT

Lattice models have been used to simulate mass transport to predict durability of cementitious materials. In particular, the use of dual lattice meshes allows for the coupling of fracture and transport processes, which commonly occur at the same time in these materials. Literature has shown good agreement between simulations and experimental results. Nevertheless, work regarding relevant computational aspects of the numerical model are scarce. In this study, a Voronoi-discretized lattice model is used to simulate unsaturated moisture transport in cement-base materials through the Richards equation. First, investigations regarding the choice of elemental volume approximation, time-stepping procedure and quadrature are evaluated . After validation of the approximations, simulated moisture transport in sound concrete was compared to experiments and mesh and time step sensitivity were discussed. A new approach to model capillary absorption of water in cracked concrete was also proposed and its advantages with respect to existing approaches are discussed by comparing to experimental measurements. The results confirm that the model can accurately predict the transport processes for the earlier stage of capillary absorption. Furthermore, moisture ingress in cracked concrete is simulated for different crack configurations and the use of different approaches is suggested accordingly. Finally, guidelines regarding the approximations used for optimization of the computations are presented.

1. Introduction

Mass transport in concrete is a significant factor in determining the durability and service life of concrete structures. The transport of fluids containing agents of deterioration can cause degradation of cementitious material and corrode the steel reinforcement. Mass transport mechanisms may influence durability of concrete structures indirectly by controlling penetration rate of aggressive agents [1]. Water acts as the major fluid that is transported within (reinforced) concrete and it can act as a carrier of chloride ions, sulphates, carbonates, or other aggressive agents that have severe unfavourable effects on concrete. Hence, it is important to understand mass transport phenomena in concrete and the various factors affecting these phenomena.

In practice, concrete is mostly unsaturated and contains cracks of different widths. These cracks are caused either by mechanical loading [2,3] or time-dependent processes such as e.g. drying shrinkage [4, 5]. Cracking accelerates the penetration of fluids and aggressive agents within the concrete which subsequently leads to faster corrosion of steel and reduces the service life of the structure [6]. Hence, studying the coupling of cracking and transport phenomena is important to predict the durability and the service life of structures. If concrete is treated

as uncracked and saturated, its service life cannot be realistically evaluated and hence, mass transport mechanisms should be considered in cracked and unsaturated concrete.

Lattice models have been used in fracture mechanics of concrete and concrete structures for several decades [7,8]. In mechanical lattice models, the continuum is discretized as a set of one-dimensional spring, truss or beam elements which transfer the load [9,10]. Such models allow simulating cracking by "removal" of broken elements in the system. This removal methodology mimics the real redistribution of stresses caused by microcracking and crack propagation in brittle materials. Such fracture model has been used with success to study all length scales in concrete and corresponding heterogeneities from hydrated cement paste [11,12], to mortar [13], to concrete [9]. Furthermore, the effect of mechanically relevant admixtures on the fracture processes of cementitious materials has been also investigated, like in reinforced concrete [14], fibre reinforced concrete [15], capsules-based self-healing concrete [16,17], etc. Moreover, different loading configurations can be simulated, as well as special boundary conditions, resulting in realistic crack paths and post-peak behaviour (i.e. compression [18], uniaxial tension [13], four-point shear [18,19],

---

etc. Analogously, tools for simulating transport processes in concrete based on the lattice modelling concept have been developed in the past two decades. In lattice transport models, the continuum is discretized as a set of one-dimensional "pipe" elements or conduits through which the transport takes place [20,21]. A two- or a three-dimensional assembly of such elements enables 2D or 3D simulation of transport in concrete, respectively. In the past, lattice transport model has been used to simulate chloride diffusion [22,23], saturated rapid chloride migration [24], saturated carbonation [25], unsaturated moisture transport [21], etc. The results of the aforementioned applications indicated the accuracy of the model to reproduce experimental results under the limited boundary and initial conditions studied.

The coupling of mechanical and transport processes in the lattice model context has been applied to the investigation of common degradation mechanisms in cementitious materials. Drying shrinkage has been simulated under certain assumptions that allow the one way coupling without including the influence of cracking on the transport [4,26,27]. Similarly many authors have used lattice model to simulate hydraulic fracture on cementitious materials, without resorting to update the transport properties as consequence of the fracture [28]. The role of cracking in transport processes such as chlorides diffusion and migration and unsaturated moisture transport have been also investigated as a decoupled problem, first cracking is simulated on the sound mesh, then the transport on the damaged mesh [22].

While the mechanical and the transport simulations are analogous, their coupling is non-trivial. In terms of coupling of mechanical and transport simulations, two approaches are possible mesh-wise. The first approach uses the same lattice mesh, in general based on Delaunay triangulation, to simulate transport and fracture phenomena. The coupling process is computationally simple, as the effects of transport processes (such as e.g. fluid pressure or differential drying) from the transport lattice can easily be converted to loads/forces acting on the mechanical lattice [27,29] thanks to concurrent node sets in both lattices. An issue arises if the effects of cracking on the transport process are to be taken into account: because the same lattice is used to simulate cracking and the transport, a transport element affected by a crack becomes perpendicular to the "real" crack, which is not physically sound. To mitigate this issue, a so-called dual-lattice approach has been proposed [30–32]. In this approach, two different but geometrically dual discretizations are used: Delaunay triangulation for the mechanical simulation, and Voronoi tessellation for the transport simulation. The dual-lattice approach allows one to naturally take the effects of cracking on transport into account, since transport elements corresponding to the cracks follow the crack geometry due to the dual nature of Delaunay and Voronoi discretizations. The main issue in the dual lattice approach arises from the non-concurrent nature of the two meshes (i.e. the mechanical and the transport mesh, respectively), resulting in a more tedious coupling procedure compared to the single-lattice approach [33]. Nevertheless, the dual-lattice approach remains very attractive.

The dual-lattice approach for simulating moisture flow in cracked concrete has shown excellent agreement with the experimental data [33]. However, since the use of a domain discretization based on Voronoi tessellation for modelling of transport processes is relatively new, comparatively little work has been done to assess computational aspects of this approach. The aim of this study is to numerically verify the effectivity of such discretization procedure to simulate transport in sound and cracked cement-based materials. First, the basics of the model, such as the spatial discretization and the weak form of the governing equation, are presented. Then, simulations of moisture transport in sound and cracked concrete are performed. Different approximations and their (numerical) implications are discussed.

2. Modelling approach

2.1. Lattice mesh generation

In the context of lattice model discretization, the domain is first divided into a number of cubic cells – voxels – with a cell size of L (Fig. 1(a)). The choice of L is determined problem by problem, taking into account the size of the smallest heterogeneities that need to be explicitly simulated, the entailed computational effort and the quality of the simulated result. Usually a mesh sensitivity analysis is performed, evaluating the results of the same problem for different L values [24,34]. Within each voxel, a sub-cell with a side length of $l = 2rL$ is defined, where r is the randomness of the mesh (see Fig. 1(b)). This sub-cell defines the region within which a node can be randomly placed. The length ratio of the sub-cell to the cell defines the degree of randomness of the lattice. The degree of randomness can vary between 0 and 0.5. When it is 0, the node is placed at the centre of each cell. When it is 0.5, the sub-cell is identical to the cell. However, in that case, a small probability exists that nodes in adjacent cells could overlap. To avoid this, the parameter r has been set to 0.2 for all simulations performed herein.

A node is then placed within each voxel. These nodes are used to define the discretization of the domain. A Delaunay triangulation and a Voronoi tessellation are performed on the nodes to partition the domain, as described in [35]. Note, again, that the two meshes are geometrically dual (see Fig. 2).

2.2. The problem of capillary moisture transport in cement-based materials

In this work, capillary moisture transport in sound concrete is simulated using the Richards equation [36]. It has been shown that the saturation form of Richards equation is convenient for describing capillary flow in unsaturated cementitious materials [23,37–39]:

$$\frac{\partial \theta}{\partial t} = \nabla(D(\theta) \cdot \nabla \theta) \qquad (1)$$

where θ is the pore water saturation [-] and $D(\theta)$ the hydraulic diffusivity$[L^2 T^{-1}]$. For undamaged cementitious materials, the hydraulic diffusivity can be approximated as [40]:

$$D(\theta) = D_0 e^{n\theta} \qquad (2)$$

where n is an empirical constant and has been demonstrated to be between 6–8, with small variability between different mix formulations [37]. Parameter D_0 can be reliably estimated from water absorption experiments as [38]:

$$D_0 = \frac{n^2 S_0^2}{(\Theta_s - \Theta_i)^2 [e^n(2n-1) - n + 1]} \qquad (3)$$

In Eq. (3), $(\Theta_s - \Theta_i)$ represents the difference between volumetric water content at saturation and at the start (related to the porosity accessible to water), while the sorptivity S_0 can be determined as the slope of the curve of cumulative water absorption vs. $\sqrt{(T)}$ measured experimentally.

The initial and boundary conditions of the described problem are as follows:

$$\theta = 1 \qquad \text{on } \Gamma_1$$
$$\frac{\partial \theta}{\partial n} = 0 \qquad \text{on } \Gamma_2$$
$$\theta(t = 0) = \theta_0 \qquad \text{in } \Omega \qquad (4)$$

In Eq. (4), Ω represents the complete domain while Γ_1 and Γ_2 are two boundaries of Ω. In addition, θ_0 is the initial moisture content in the concrete.

Eq. (1) can be discretized in space using the standard Galerkin approach [41], resulting in:

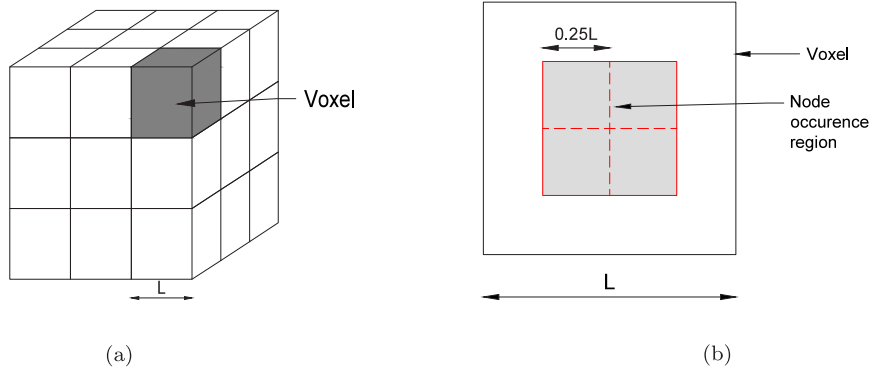$$M\frac{\partial \theta}{\partial t} + K\theta = F \qquad (5)$$

Fig. 1. (a) Division of domain into voxels; (b) Region of occurrence within a voxel with a randomness of 0.25.
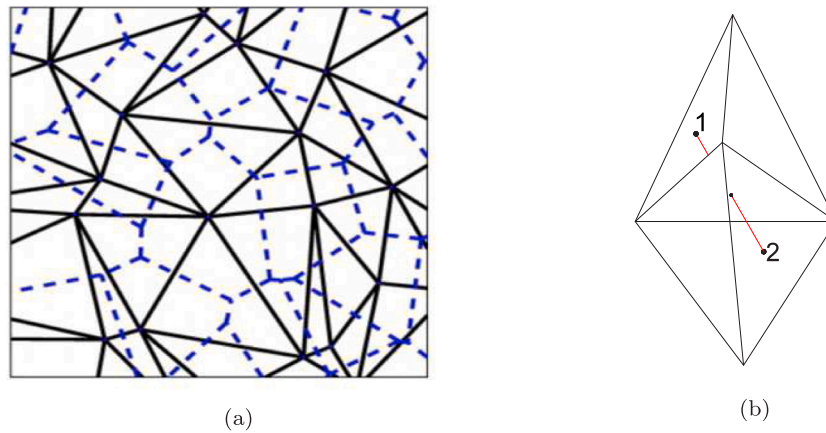

Fig. 2. (a) Meshing procedure (shown in 2D for simplicity). Solid — lattice mesh; dashed — Voronoi tessellation (adapted from [22]); (b) (in 3D) Voronoi element (1–2), connecting nodes in two adjacent Delaunay tetrahedra.

In Eq. (5), M and K are the mass and diffusivity matrices, respectively, while F is the forcing vector capable of handling boundary conditions of Neumann type (which are nil in the studied problem and thus are directly satisfied). For generic boundary conditions each element $i - j$, mass and diffusivity matrices and the forcing vector are defined as:

$$m_{ij} = \frac{A_{ij} l_{ij}}{6} \begin{bmatrix} 2 & 1 \\ 1 & 2 \end{bmatrix} \qquad (6)$$

$$k_{ij} = \frac{A_{ij}}{l_{ij}^2} \begin{bmatrix} 1 & -1 \\ -1 & 1 \end{bmatrix} \int_L D_{ij}(\theta) dx \qquad (7)$$

$$f_{ij} = \begin{bmatrix} f_i \\ f_j \end{bmatrix} \qquad (8)$$

Here, A_{ij} and l_{ij} are the cross-sectional area and the length of a lattice element, respectively. In this work, Eq. (5) is discretized in time using the Crank–Nicolson procedure [41]:

$$(M + \tfrac{1}{2}\Delta t K^{n+1})\theta^{n+1} = (M - \tfrac{1}{2}\Delta t K^n)\theta^n + \Delta t f \qquad (9)$$

2.3. Approximations

In modelling the capillary absorption of moisture in concrete we have resorted to simplifications with the aim of reducing the computational demand. Such approximations are introduced in this section. The evaluation of the errors incurred on as a consequence of the aforementioned simplifications are addressed later in the following sections.

2.3.1. Volume approximation

The correct assessment of the volume of the discrete elements is necessary for respecting the law of mass conservation. Using the dual Delaunay tetrahedra as auxiliary mesh, it is possible to define the exact volume ascribed to Voronoi elements within the lattice mesh. Each Voronoi element passes through the common facet of two adjacent Delaunay tetrahedra within which the two nodes of the element are located, as shown in Fig. 2(b). Such element entails volume fractions from both tetrahedra, resulting in a smaller Voronoi tetrahedron (Fig. 3(a)). The latter are formed by joining the Voronoi nodes with the three Delaunay nodes that form the common triangle.

Alternatively, the volume of a Voronoi element can be approximated by considering that the area of the common Delaunay triangle extends throughout the length of the Voronoi element [30] as shown in Fig. 3(b). In this case, an overlap between two corresponding Voronoi elements occurs. This overlap can be accounted for by modifying the element mass matrix (given by Eq. (6)) using a correction factor ω [20]:

$$m_{ij} = \frac{A_{ij} l_{ij}}{6\omega} \begin{bmatrix} 2 & 1 \\ 1 & 2 \end{bmatrix} \qquad (10)$$

where:

$$\omega = \frac{\sum A_{ij} l_{ij}}{V} \qquad (11)$$

In Eq. (11), V is the total volume of the considered domain.

Using the exact volume is comparatively complex to be included in the numerical model as the volume of each sub-tetrahedra must be calculated. Instead, the approximated volume is used for the analysis in the numerical model. Herein, ω is taken to be equal to 3, as suggested by Bolander and Berton [20] for 3 dimensional simulations.
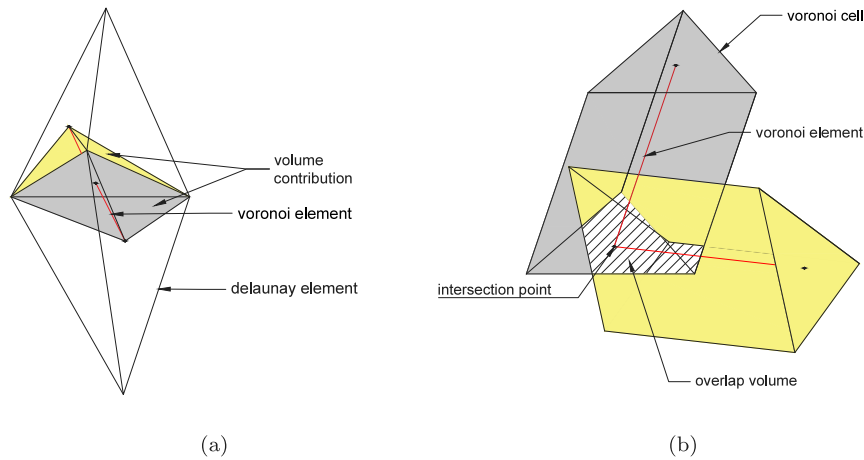
Fig. 3. Volume of the Voronoi elements.

2.3.2. Linearization of the time-stepping procedure

It can be seen from Eq. (9) that, in order to compute the saturation θ_{n+1} at the end of each time interval Δt, the diffusivity matrix at the end of the same time step (i.e. K_{n+1}) should also be known. This means that the time-stepping procedure is implicit, and in each time step, two unknowns must be determined: θ_{n+1} and K_{n+1}. This can be done by utilizing an iterative solution procedure such as a Newton–Raphson scheme. Alternatively, a linear approximation can be used to solve Eq. (9), which circumvents the need for an iterative procedure [3,27, 39]. In that case, instead of using the diffusivity matrix at the end of the time-step (K_{n+1}), the diffusivity matrix at the beginning of the time step (K_n) is used. Therefore, Eq. (9) can be simplified as:

$$(M + \frac{1}{2}\Delta t K^n)\theta^{n+1} = (M - \frac{1}{2}\Delta t K^n)\theta^n + \Delta t f \tag{12}$$

Eq. (12) presents an explicit form of the time stepping scheme which does not depend on information at time t_{n+1}. Therefore, it can be solved directly.

Using an explicit time stepping scheme has consequences on the stability and the accuracy of the results which are analysed later. The Crank–Nicolson procedure, used for time discretization of the semi-discrete form of the governing equation, is considered to be unconditionally stable. The linearization procedure, as described above, results in a loss of unconditional stability of the scheme. In each time step, an error is induced in the solution, the magnitude of which depends on the magnitude of the time step. This error can accumulate with the accession of the time steps and the solution can diverge rapidly from any realistic results causing instability. Hence, the magnitude of the time step should be sufficiently small so that the error induced does not cause instability.

2.3.3. Uniform mean diffusivity

Calculation of the diffusion matrix of an element requires the computation of the integral of the diffusivity along the length of the element as given by Eq. (7). The diffusivity varies exponentially with the saturation level [23]. Using spatial discretization, the saturation level in the domain is discretized and varies linearly along the element length. Extending the discretization to diffusivity, it varies exponentially over the element length as:

$$D = D_c e^{n_c x} \tag{13}$$

where

$$D_c = D_0 e^{n\theta_i} \tag{14}$$

$$n_c = \frac{n}{L}(\theta_j - \theta_i) \tag{15}$$

The integral of diffusivity, over the length of the element is evaluated more accurately if the total area under the curve is considered as shown in Fig. 4(a). The area can be estimated using 4-point Gauss-integration as:

$$k_{ij} = \frac{A_{ij} D_0 e^{n\theta_1}(e^{n(\theta_j - \theta_i)} - 1)}{n l_{ij}(\theta_j - \theta_i)} \begin{bmatrix} 1 & -1 \\ -1 & 1 \end{bmatrix} \tag{16}$$

The approach is commonly simplified by approximating the diffusivity integral with a trapezoidal rule [3,27,39]. In that case, the diffusion matrix of each element is calculated as:

$$k_{ij} = \frac{A_{ij} D_0 e^{0.5n(\theta_i + \theta_j)}}{l_{ij}} \begin{bmatrix} 1 & -1 \\ -1 & 1 \end{bmatrix} \tag{17}$$

The implications of using Eq. (17) instead of Eq. (16) are discussed later.

2.4. Approach validation for constant diffusivity

To validate the moisture transport model, Eq. (9) was solved numerically, as described before. Two benchmark problems, for which constant unitary diffusivity was assumed, were simulated and the outcome was compared to the analytical solution. The same cubic domain of $10 \times 10 \times 10$ mm³ was used in both benchmark cases with a voxel size of 0.5 mm. The boundary conditions of the problems are reported in Fig. 5a and 6a for steady-state flow case and non-stationary flow, respectively.

Regarding the steady-state benchmark case, it is expected that a linear change of the moisture potential between 0 and 1 should be obtained. The accuracy of the numerical solution is assessed through two error norms:

$$\|r\|_{\infty} = max|r_n|, n = 1...N \tag{18}$$

$$\|r\|_2 = \sqrt{\frac{1}{N}\sum_{n=1}^{N}|r_n|^2} \tag{19}$$

Here, N is the total number of nodes in the domain and r_n the difference between the theoretical and calculated moisture content for node i. The error norms have been calculated as 0.0153 and 0.0043 for the $\|r\|_{\infty}$ and $\|r\|_2$, respectively, which is considered acceptable for the present application.

To validate the performance of the model in the case of non-stationary flow, a problem presented in [30] is used with unitary time step. The initial saturation of the nodes within the domain is given as:

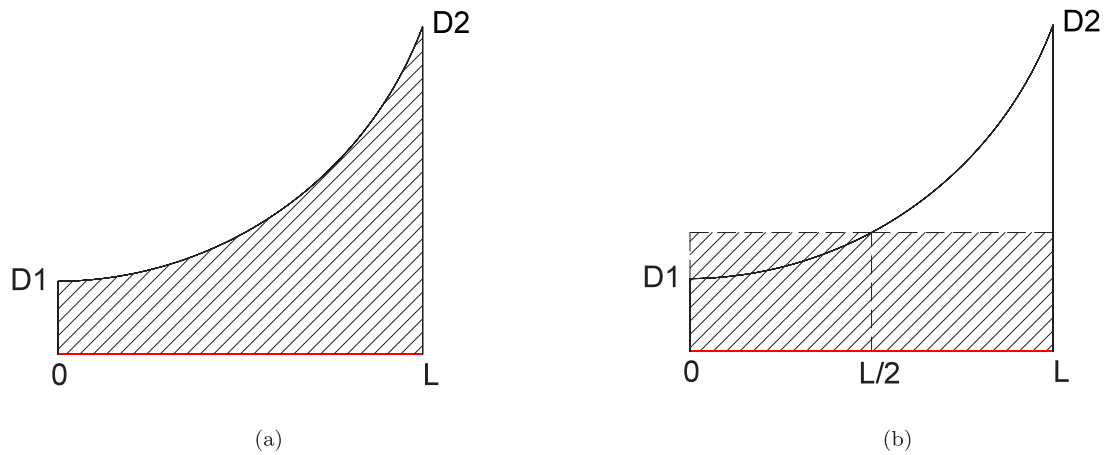$$\theta_i = \theta_0 sin(\frac{\pi x}{L}) \tag{20}$$

Fig. 4. Variation of diffusivity over the element: (a) 4-point Gauss integration of diffusivity; (b) 1-point Gauss integration of diffusivity.
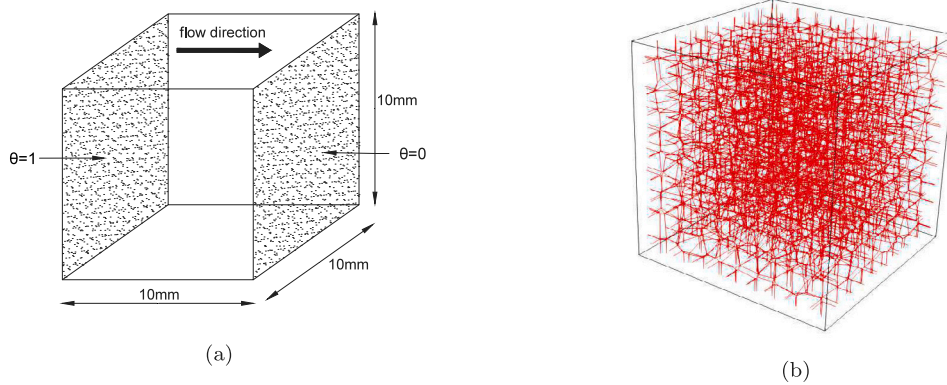

Fig. 5. Cubic domain subjected to steady state flow: (a) Flow conditions in the domain; (b) Domain discretization using Voronoi elements.
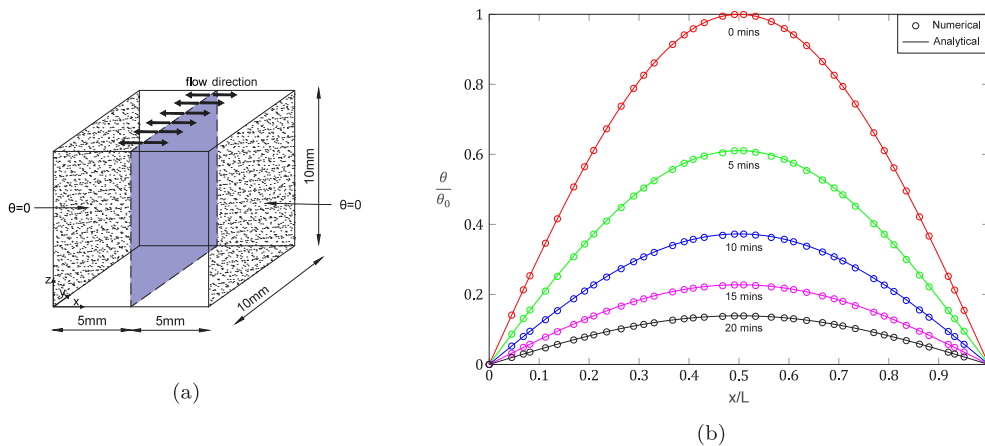

Fig. 6. Cubic domain under non-stationary flow. (a) boundary conditions; (b) comparison between the numerical and the analytical solution.

The analytical solution of the problem is given as [20]:

$$\theta(x,t) = \theta_0 sin(\frac{\pi x}{L})e^{(\frac{\pi^2}{L^2}t)} \qquad (21)$$

A comparison between the analytical and the numerical solution is given in Fig. 6b. It can be seen that the results of the model match the analytical solution very well.

2.5. Coupling of mechanical and transport models

The main benefit of using the dual-lattice approach, compared to the single lattice approach, is for simulating transport in cracked concrete. When a single lattice approach is used, the same lattice mesh is used to simulate both the mechanical problem and the transport problem. In sound concrete, this is not an issue: the Delaunay approach correctly
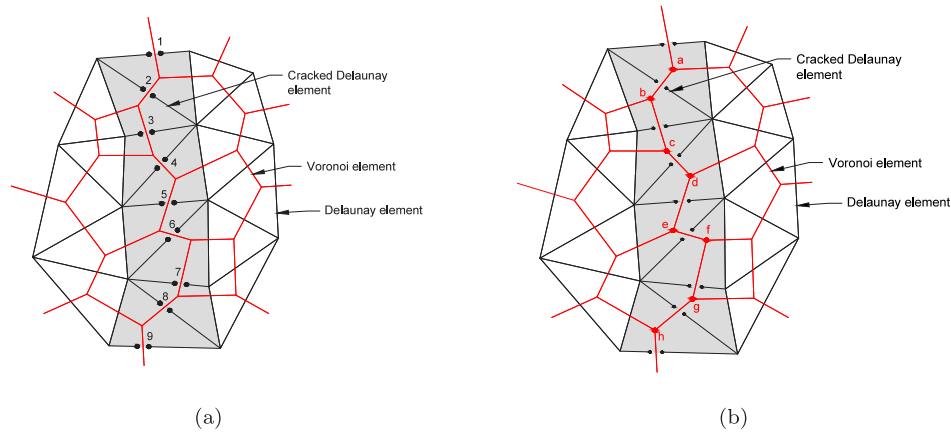
Fig. 7. Approaches for simulating moisture transport in cracked concrete using the lattice approach. (a) single lattice approach using Delaunay elements, where the damaged elements (1–9) from the mechanical problem are also used to simulate moisture transport in cracks; (b) dual lattice approach, in which transport in cracks in simulated using Voronoi elements (a–h) dual to the Delaunay elements damaged in the mechanical problem.
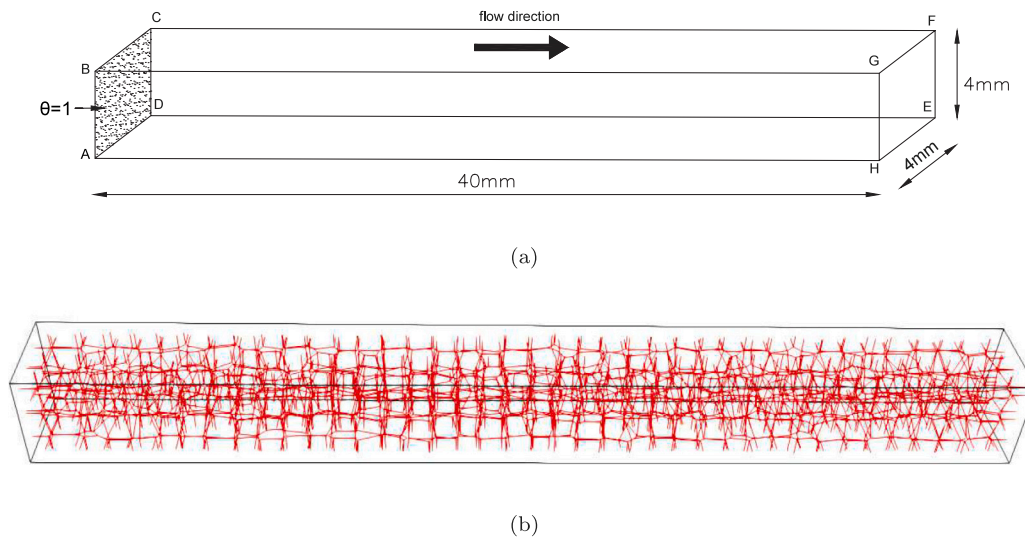

Fig. 8. Description of the numerical model for simulating the non-steady state flow.

discretizes the complete domain and preserves the volume. If a crack occurs, however, a problem arises: in the lattice approach, this is simulated by damaging or removing the Delaunay elements. If the same mesh is used to simulate transport, then the transport elements in cracks are positioned perpendicular to the simulated crack, which is not physically correct (see Fig. 7a). On the other hand, if the dual Voronoi–Delaunay lattice approach is used, the transport elements in the crack region naturally follow the crack path due to the duality between the Delaunay triangulation and the Voronoi tessellation (see Fig. 7b). In Section 4, the use of the dual-lattice approach for simulating moisture transport in cracked concrete is presented.

3. Moisture transport in sound concrete

3.1. Experiment and model

The model was used to simulate the experiment performed by Zhang et al. [42]. In the experiment, moisture transport in an uncracked mortar sample of dimensions $100 \times 50 \times 20$ mm^3 was monitored by means of neutron radiography. A water–cement ratio of 0.6 and a mortar mix proportion of 1:3.3:0.6 (cement:sand:water) by volume was used. After curing for 14 days, the specimens were dried in an oven for 4 days at a temperature of 50°, until attaining constant weight.

Unidirectional moisture flow was ensured by sealing all surfaces except the exposed surface with self-adhesive aluminium foil. The exposed surface (dimensions 100×20 mm^2) was submerged in water, and moisture distribution was measured for 8 h using neutron radiography. The immersion depth was around 5 mm

The required input D_0 was calculated using a theoretical formulation derived by Wang [43], in which the capillary coefficient k is related to the sorptivity S_0 and to the porosity of the material Θ_s considering an initially nearly dry material ($\theta_0 = 0.01$) as shown in (22):

$$k = 1.294 \frac{S_0}{\Theta_s} \tag{22}$$

Where k is the slope of the moisture penetration depth vs. square root of time curve [44]. This can be experimentally measured if the wet front position is known over time or calculated if the coefficient of capillary suction and the water capacity of the material are known, as detailed in [45]. As in [23], by substituting S_0 from Eq. (22) in Eq. (3), the following relationship is obtained between k and D_0:

$$D_0 = \frac{(k/1.294)^2}{123.131} \tag{23}$$

Note that in performing this substitution, the Θ_s is eliminated and thus k (which depends on the porosity and sorptivity of the material) carries over this information for the calculation of D_0.
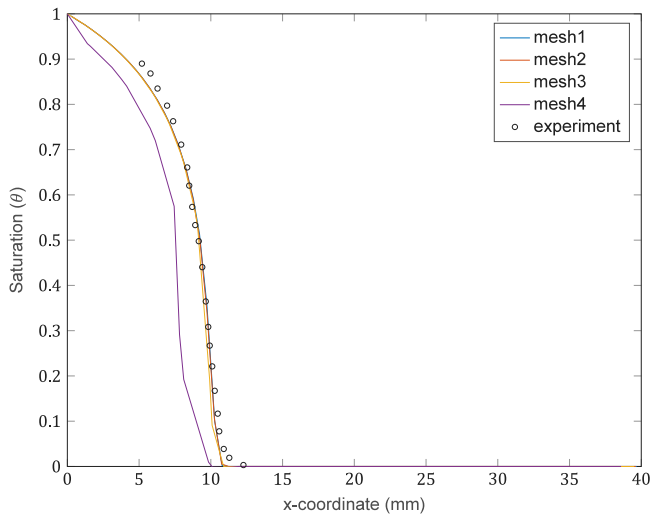
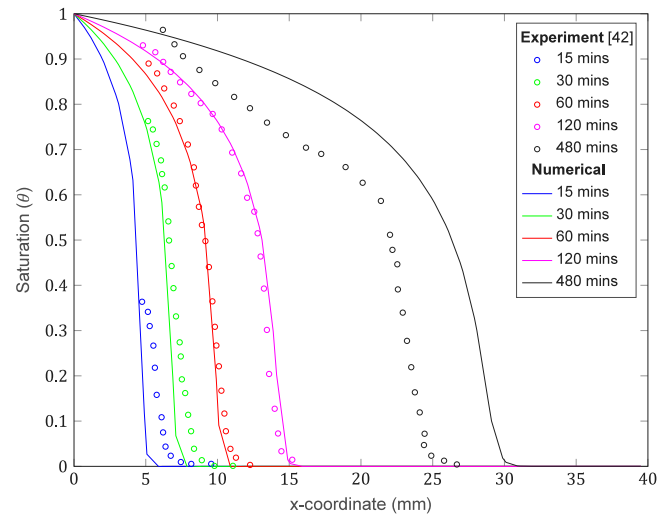**Fig. 9.** The influence of mesh size on simulated moisture profiles.

Fig. 10. Comparison between experimental and numerical moisture profiles at different time intervals (for mesh 3).

Table 1
Parameters used in the default simulation of flow in non-saturated mortar.

Parameter	Symbol	Value
Diffusivity of dry mortar $[mm^2/s]$	D_0	1.5467×10^{-4}
Empirical constant [-]	n	6
Initial saturation [-]	θ_o	0
Porosity [-]	p	0.0462
Time step [s]	δt	6

Based on the reported value of the capillary coefficient $k = 10.714$ mm/h$^{1/2}$ for the studied mortar [23,42], the diffusivity is estimated as $D_0 = 1.54676 \times 10^{-4}$ mm^2/s.

For the simulations, a Volume of Interest (VOI) of $40 \times 4 \times 4$ mm^3 was used to limit the computational effort (Fig. 8a). The domain was discretized using Voronoi elements and uni-directional flow was simulated (Fig. 8b). All input parameters are given in Table 1.

3.2. Mesh sensitivity analysis

Using the flow parameters, boundary and initial conditions as mentioned above, the analyses were carried out using four different characteristic mesh element sizes, described in Table 2. The simulation results and the experimental moisture profiles after 60 min of capillary water absorption are shown in Fig. 9.

It can be seen that the simulated results using meshes 1 to 3, are relatively similar to the experimental ones. Instead, for the coarsest mesh, 4, the simulated moisture profiles deviated substantially from the experiments. The same trend holds for all time intervals. In further analyses, mesh 3 is therefore used.

In Fig. 10, a comparison between the simulation results (with Mesh 3) and the experimental data for different times is given. It can be seen that, at 15 min, the numerical results underestimate the moisture penetration depth and content compared to the experiment. The reason for the mismatch at early stages of capillary water absorption is that experimental samples often have a so called wall effect. This effect alludes to the presence of air voids and the decrease of aggregates volume fraction in proximity of cast mortar surfaces which correlates greatly with initial fast uptakes of water during sorptivity tests as elucidated [40]. In fact after 30, 60 and 120 min the numerical results compare well with the experimental results. Then again at 480 min the moisture penetration depth is overestimated by the numerical model. There can be various hypotheses that explain this discrepancy. First
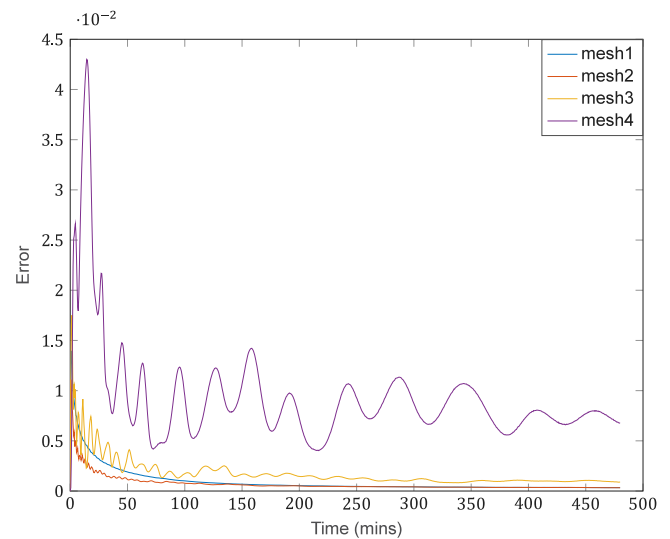

Fig. 11. Error vs elapsed time graph for volume approximation.

of all, in this work the diffusivity is considered uniform throughout the domain, but in reality mortar is heterogeneous in nature and the influence of impermeable aggregates is not constant in different parts of the domain. With the advancement of flow, the influence of mortar heterogeneity increases. This heterogeneity is not accounted for in the numerical model and instead, a uniform diffusivity throughout the domain is considered which may cause a deviation between the experimental and the numerical results. Secondly, it has been discussed in previous studies [46] that the sorptivity curves, from which the diffusivity values are derived, present a marked plateau at later stages during capillary moisture absorption, especially in large and/or highly porous samples, where the effects of gravity may dampen those of the capillarity forces. Finally, other researches [47] have reported progressive decrease of water uptake due to the swelling of cement hydrates during experimental capillary absorption of moisture in mortar. The latter two hypotheses cite phenomena that are not taken into consideration when the hydraulic potential is solely described by the value of the diffusivity at early stages and therefore, their effect cannot be captured in the numerical simulations.

Table 2
Properties of meshes used for studying the effects of mesh size dependency.

Mesh	Number of nodes [-]	Number of elements [-]	Mean element length [mm]
Mesh 1	62028	112878	0.1757
Mesh 2	30859	54786	0.2231
Mesh 3	3333	5208	0.4792
Mesh 4	280	329	1.1306

(a)   (b)
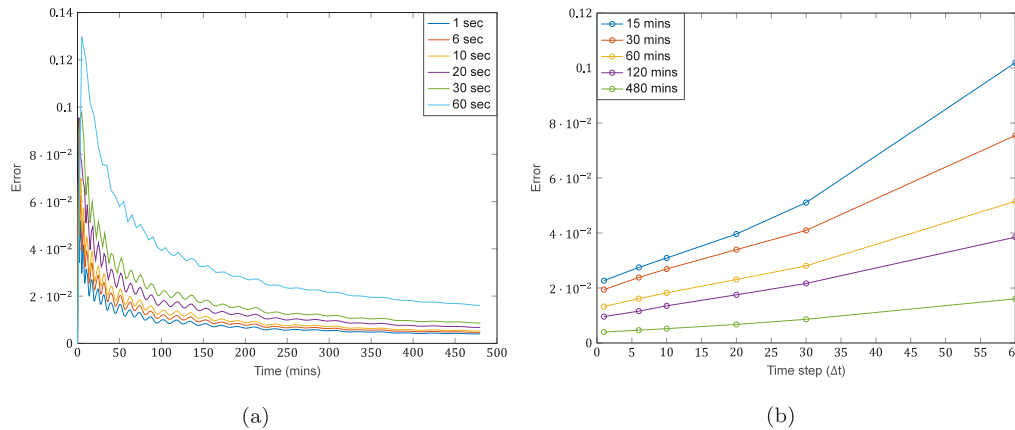
Fig. 12. Error vs Time graph for explicit vs. implicit solver.

3.3. Validity of approximations

3.3.1. Approximate volume

Simulations performed using the exact volume (Fig. 3a) were compared to the results simulated using the approximated volume (Fig. 3b) by calculating the error between the saturation levels for the two analyses at each time step using the L-2 error norm which is given by Eq. (19). The analyses were carried out on the 4 meshes given in Table 2, and the results are reported in Fig. 11.

It can be seen that for all meshes, the global behaviour is such that the error decreases with time, showing the stability of the volume approximation considered. Generally, at a given time, the magnitude of the error is smaller for a finer mesh, although this trend does not hold when comparing meshes 1 and 2. The latter is due to the fact that the number of elements in mesh 1 is higher than in mesh 2. When the volumetric capacity of the domain (M matrix) is computed for all elements using the approximate (mean correction factor) and the exact approach, the error per element is lower for mesh 1 as it is the finer mesh. However, as the error norm is calculated as sum of nodal errors, the finer mesh, having more nodes, shows a larger error. Hence, further mesh refinement might not lead to more accurate results when the approximated model is used.

The local and global behaviour of the error vs time graph (Fig. 11) can be explained by the transitional behaviour of the flow in the discretized domain. The global behaviour of the graph is such that the error is reducing with time. The approximate volume model uses the average correction factor ω (Eq. (11)) on all individual elemental volumes, because of which, the volume of individual elements is not accurate but the total volumetric capacity is the same as the exact volume of the domain. During the initial time stages, the predominant flow in the domain is limited to a relatively small fraction of elements. When the approximate volume of such small amount of elements is used for the simulations, it gives a higher error because such volume is being computed using a correction factor based on a much bigger data set comprising all the elements in the domain. As the flow continues, the water front travels in the direction of the flow, involving more elements. Consequently, the error in saturation level decreases as the approximated cumulative volumetric capacity approaches the exact volume.

It can be observed in Fig. 11 that the error does not decrease gradually but there are local peaks. The frequency of these peaks becomes higher and the magnitude of the local maximum becomes lower as the mesh becomes finer, which suggests that the behaviour of these local peaks is highly mesh-dependent. The nature of flow in the domain is such that the moisture is not spread uniformly over the entire domain but it accumulates in the nodes that are enveloped by the wetting front. After the accumulation of moisture, it then spreads over to the adjacent nodes in the direction of the flow. As the water front moves forward in this direction, it continually involves more elements and leaves saturated elements behind. The elements at the penetration front have one node whose saturation is close to fully-saturated condition and the second node saturation closer to the initial saturation. Local peaks in the error vs time graph occur when new elements are being introduced in the flow. The time at which the error starts increasing is that at which one of the nodes of the penetration front elements is close to complete saturation and the second node is close to the initial saturation. As these elements are enveloped by the penetration front, the saturation of the second node gradually increases. Notwithstanding, due to a difference in the volumetric capacity of the elements computed from both the models, the two saturation levels of the second node will differ. Globally the error is reduced in time, but due to the former difference in saturation of the second node in different models, the variation of diffusivity over the element for each model is different. As flow progresses, the difference of saturation levels of the second node increases further and the error increases (local peaks). At a certain point, as the second node becomes more and more saturated, the difference in the diffusivity decreases and, eventually, the increase in error due to local differences in diffusivity is compensated by the decrease in the global error. After this point, the decrease in error because of volume approximation becomes the predominant factor. The whole process is then repeated in the next set of elements in the proximity of the penetration front. The frequency of the peaks is higher in a fine mesh because there are more elements. Moreover, the amplitude of the peaks decreases as the mesh is refined because the magnitude of the difference in volumetric capacity and the diffusivity variation decreases, thus the error in the saturation levels.
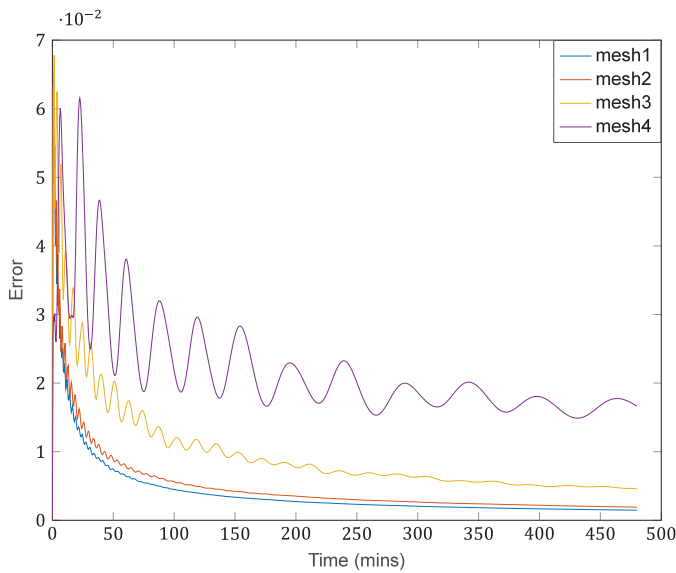
Fig. 13. Error vs Time graph for diffusivity approximation.

3.3.2. Linearization of the time-stepping procedure

Herein, an implicit time stepping scheme is used to more accurately solve the discretized equation. The biconjugate gradient stabilized method (BiCGSTAB) [48] was used to solve the equation iteratively. The tolerance of the scheme is set to 10^{-6} and the L-2 error norm is used to compute the error in the saturation levels between the explicit and implicit time stepping schemes results. Fig. 12a shows the error vs elapsed time graph at six different time steps during the simulated capillary absorption of water. It is clear that the error increases with larger time steps. The graph is similar for different time steps, the only difference being the magnitude of error at different time stages.

As can be seen in Fig. 12a, the error (for all time steps) is decreasing with time showing that the explicit model is stable. But it can be seen in Fig. 12b that the error increases for larger time steps, thereby decreasing the accuracy of the explicit model.

3.3.3. Estimated diffusivity

Four-point Gauss quadratures are used in the numerical integration of the diffusivity (see Fig. 4). The model using such approach is run on 4 different meshes as presented in Table 2. The L-2 error norm vs. time is given in Fig. 13.

Clearly, the finest mesh produced the most stable and accurate results. The overall behaviour is similar to the one observed for volume approximation (Fig. 13), and can be explained in a similar fashion. Globally, the error decreases with time. This is due to the fact that as time progresses and the water front moves forward in the direction of the flow, more nodes become completely saturated. In an element where both of its nodes are completely saturated, the diffusivity remains constant over the length of the element and the numerical integration of the diffusivity approaches its exact integral. Eventually, when all nodes are completely saturated, the diffusivity of the entire domain for both methods will be equal. It should be noted also that a smoother decrease of the error with time is observed for finer meshes, as expected.

Overall, it can be said that if a sufficiently fine mesh and time step are used in the analyses, the error due to the use of 4-point gauss quadrature discussed above is acceptable.

4. Moisture transport in cracked concrete

4.1. Capillary moisture uptake in cracks

The capillary suction in the crack happens in a matter of seconds in which the equilibrium height is obtained, while the process of moisture transport in the adjoining matrix is slower. Because of this, the coupling of these two phenomena in a single numerical model is complex. Therefore, herein, first the capillary suction in the crack is modelled, then considering the crack walls as additional submerged boundaries, the transfer of moisture in the adjoining cement matrix is simulated using a separate numerical model. Moisture rise in a capillary can be simulated using a modified Lucas–Washburn equation, as proposed by Gardner et al. [49]:

$$\left(\frac{2\beta_m}{r} + \frac{z}{\frac{r\beta_w}{2} + \frac{r^2}{8\mu}}\right)\dot{z} = p_{c0}(1 - \beta_s) - \rho g z \sin(\phi) \tag{24}$$

where β_m is the correction factor for dynamic contact angle, r is the radius of the capillary, z is the capillary rise, β_w the correction factor for the wall slip, μ the dynamic viscosity, β_s the correction factor for the stick–slip behaviour, ρ the density of the liquid (water), ϕ the inclination angle of the capillary, g the acceleration due to gravity, p_{c0} the capillary pressure, determined as:

$$p_{c0} = \frac{2\gamma \cos(\alpha_0)}{r} \tag{25}$$

where γ is the surface tension and α_0 is the liquid–solid contact angle.

Eq. (24) gives the expression for the rate of capillary rise in a capillary. This equation is discretized in time using the Crank–Nicolson procedure as:

$$z_{n+1} = z_n + \frac{\Delta t}{2}(\dot{z}_n + \dot{z}_{n+1}) \tag{26}$$

For simplicity, we can define the following constants:

$$k_1 = \frac{2\beta_m}{2} \tag{27}$$

$$k_2 = \frac{r\beta_w}{2} + \frac{r^2}{8\mu} \tag{28}$$

$$k_3 = p_{co}(1 - \beta_s) \tag{29}$$

$$k_4 = \rho g \sin(\phi) \tag{30}$$

Now, substituting Eq. (26) into Eq. (24) and eliminating the time derivatives, the discretized form of Lucas–Washburn equation is obtained as:

$$\frac{2}{\Delta t}z_{n+1}^2 + \left(\frac{2}{\Delta t}k_1 k_2 - \frac{2}{\Delta t}z_n - \frac{k_2 k_3 - k_2 k_4 z_n}{k_1 k_2 + z_n} + k_2 k_4\right)z_{n+1} - \left(\frac{2}{\Delta t}k_1 k_2 z_n + \frac{k_1 k_2 (k_2 k_3 - k_2 k_4 z_n)}{k_1 k_2 + z_n} + k_2 k_3\right) = 0 \tag{31}$$

When the surface of concrete is in contact with water, the crack acts as a capillary tube. Due to surface interactions with the moisture present at the submerged boundary, the water rises up in the capillary, and stops when the capillary attains equilibrium height. The height up until which the crack gets filled up acts a boundary with constant saturation and the moisture starts spreading into the adjoining matrix through the crack walls as shown in Fig. 14.

For the case of a planar crack (Fig. 14a), capillary suction is simulated directly using the modified Lucas–Washburn equation (Eq. (24)) as the crack width is uniform throughout the depth of the crack. Once the equilibrium height is attained, the moisture starts spreading into the adjoining matrix. On the other hand, when the crack width is not uniform, but varies with the crack depth, i.e. a wedge-shaped crack as shown in Fig. 14b, the crack is divided into a number of discrete elements. The crack width is assumed to be constant for each discrete element and the capillary suction is modelled using the discretized form
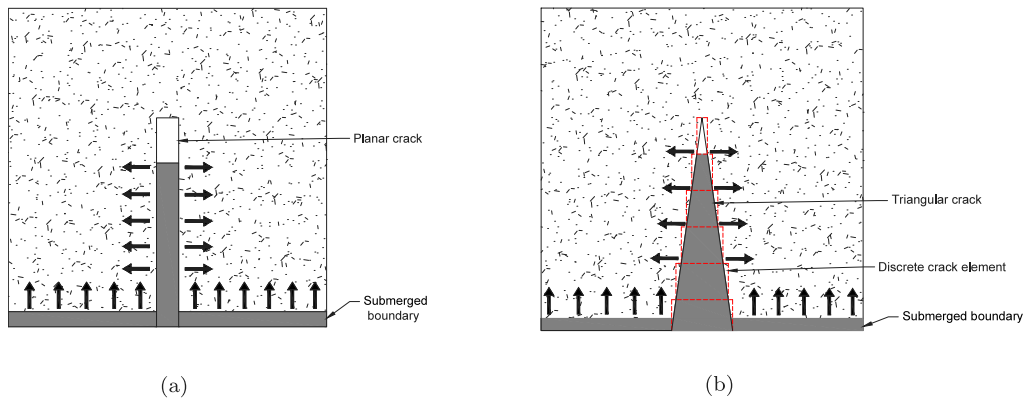
Fig. 14. Capillary suction in the crack: (a) planar crack; (b) V-shaped (tapered) crack.
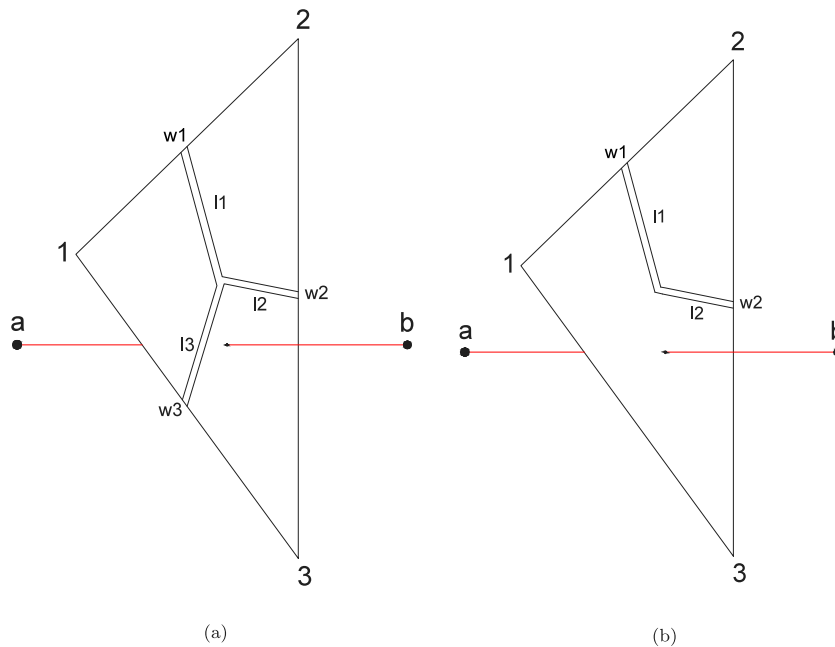

Fig. 15. Equivalent crack properties of the Voronoi element: (a) Voronoi element surrounded by three cracked Delaunay elements; (b) Voronoi element surrounded by two crack Delaunay elements.

of the Lucas–Washburn equation. Due to capillary suction, the water in the crack reaches an equilibrium height but if the crack depth is greater than the equilibrium height, a part of the crack is left which is not filled with water. This part is considered to have the moisture transport being dependent on the crack width through the so-called cubic law [23]:

$$D_w^{cr}(\theta) = (\sum_{i=1}^{n} w_i^3 l_i) \frac{\xi p_r (1-m)}{12 \mu A m} \sqrt{\theta} [1 - (1 - \theta^{1/m})^m]^2 \theta^{-1/m-1} (\theta^{-1/m} - 1)^{-m}$$

(32)

where w_i is the equivalent crack width, l_i the equivalent crack length, n the number of cracked Delaunay elements, A the cross-sectional area of the Voronoi element, ξ the tortuosity factor, p_r the reference pressure (experimentally determined as 18.6237 N/mm^2, m the van Genuchten parameter (0.4396) and μ the viscosity of water. For the Voronoi elements that are in the crack but beyond the area of capillary rise, Eq. (32) is used to calculate the diffusion coefficient for assembling the diffusivity matrix.

The equivalent crack widths and the equivalent crack lengths can be computed for a Voronoi element as shown in Fig. 15a [31]. The Voronoi element a-b is surrounded by three Delaunay elements 1–2, 2–3 and 3–1 that form the common triangle. When the Delaunay

elements are cracked, the crack widths w_1, w_2 and w_3 are assumed to be present in the middle of the corresponding elements. The crack lengths l_1, l_2 and l_3 are obtained by calculating the distance from the centre of the corresponding Delaunay elements to the centroid of the common triangle 1-2-3. The cross-sectional area A of the Voronoi element is the area of the triangle 1-2-3. When cracking is simulated in three dimensions, the Delaunay elements lying in the cracked plane are considered to be cracked. Due to the fact that these elements are lying in a plane, it is never the case that a Voronoi element passes through three cracked Delaunay elements as shown in Fig. 15a. Instead, the maximum number of cracked Delaunay elements that pass through a Voronoi element is two, as shown in Fig. 15b. In such a case, the Voronoi element lies partly in the crack and partly in the uncracked region and its' diffusivity should be considered as the weighted average of the diffusivity of the cracked and the uncracked region. But the contribution of the uncracked region towards the diffusivity is considerably smaller as compared to that of the cracked region and only the cracked Delaunay elements (1–2 and 2–3 as shown in Fig. 15b) are used to assign the diffusivity of the Voronoi element.

Note that from this point on to simulate moisture transport in cracked concrete a numerical model using approximate volume of
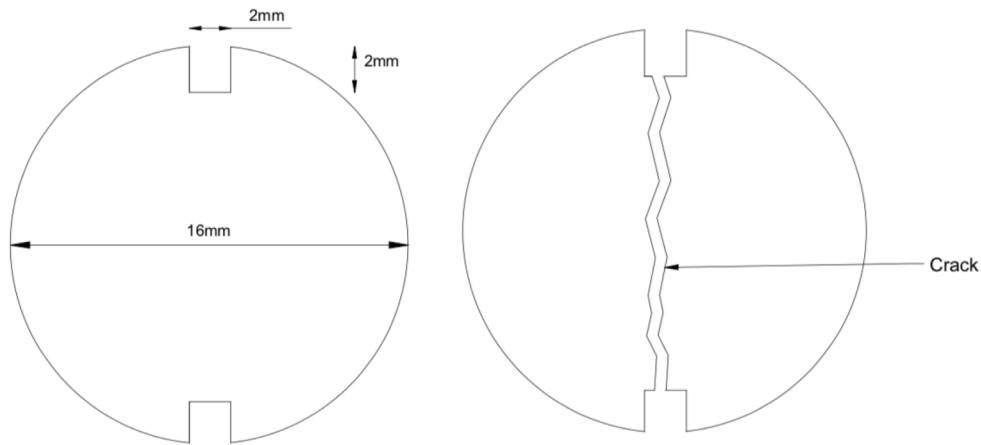
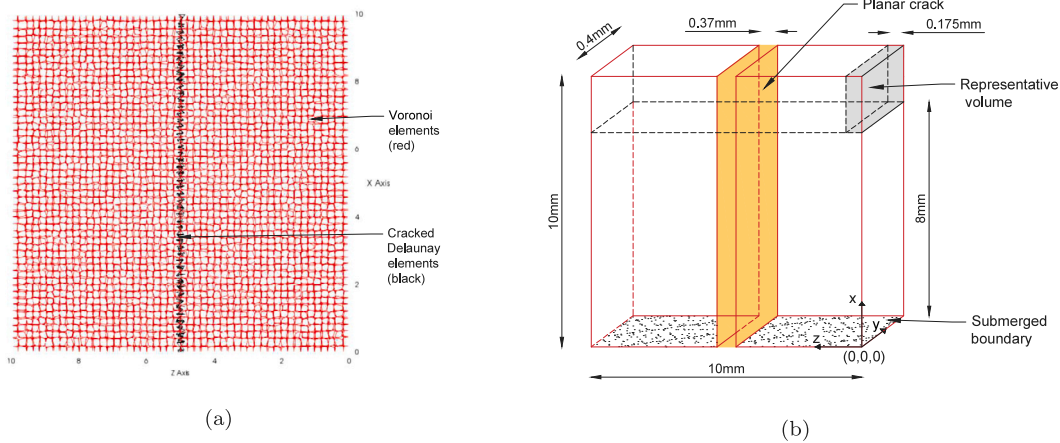**Fig. 16.** Schematic of the sample and the crack [50].

(a)

(b)

Fig. 17. Description of the numerical model: (a) Voronoi mesh for transport, together with Delaunay elements in the crack; (b) geometry and boundary conditions.

the Voronoi elements, explicit time stepping technique and diffusivity evaluated for the mean saturation of the element is adopted.

4.2. Moisture transport in parallel-walled cracks of uniform width

4.2.1. Experimental details

The experiment used in [50] is used as a reference to simulate horizontal moisture distribution in cracked mortar. In the experiment, a cylindrical specimen of 16 mm diameter and 32 mm height was used. The mortar cylinder was provided with two grooves of 2 mm width and 2 mm height placed diametrically opposed, as shown in Fig. 16. The water–cement ratio was 0.45 and the cement to sand ratio was 3.27.

At 28 days of age, the sample was put in an oven at 40° until constant weight was achieved. The sample was then split in a Brazilian tensile test configuration. Metallic inserts with nominal width of 2.3 mm were used to steer a nominal crack width of 0.3 mm in the split sample, which was glued back together by means of two-component glue. The resulting crack had an average width of 0.37 mm. The samples had a uniform initial saturation at the time of testing. X-ray Micro Tomography was used to monitor the moisture distribution at different time stages during a capillary water absorption test [50]. Although the sample crack was rough and tortuous, the 3D data has been arranged to have the centre of the crack for each depth and height in the same position. This results in a planar crack where the crack width could be considered constant.
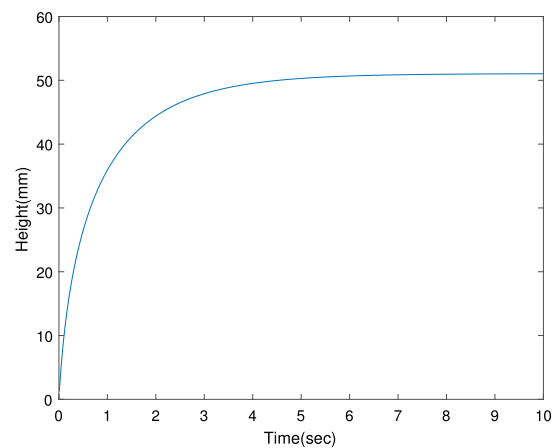

Fig. 18. Capillary rise in the crack.

4.2.2. Numerical analysis

For the numerical analysis, a cracked domain was generated to simulate the moisture distribution as given in the experiment. A dual mesh with domain sizes and mesostructure as reported in Fig. 17a was first modelled on the Delaunay elements. The average Delaunay element size was taken as close to the crack width as possible to be representative of the actual crack width as used in the experiment. The mesh characteristics are reported in Tables 3 and 4 as well as the flow
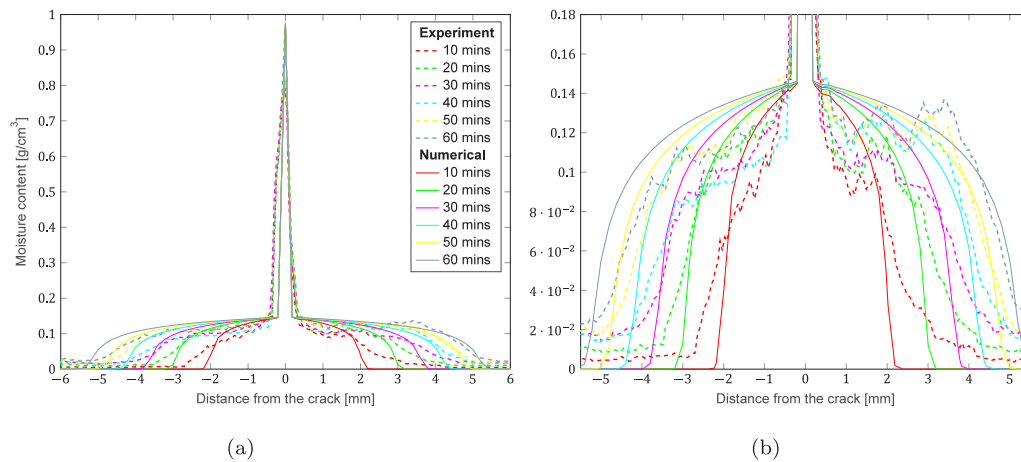
Fig. 19. Experimental and numerical moisture profiles perpendicular to the crack for parallel walled cracks: (a) full profiles including crack moisture content and (b) zoom in on the mortar phase moisture content.

Table 3
Mesh Properties.

Parameter	Value
Number of nodes [-]	26225
Number of elements [-]	37456
Mean element length [mm]	0.1
Crack width [mm]	0.3719
Crack depth [mm]	10

Table 4
Flow Parameters.

Parameter	Symbol	Value
Diffusivity of dry mortar [mm^2/s]	D_0	3.5×10^{-5}
Empirical constant [-]	n	6
Initial saturation [-]	θ_0	0.2119
Porosity [-]	p	0.1471
Time step [s]	Δt	6

parameters used to simulate moisture transport in the sound mortar domain. The flow parameters were available from unpublished measurements[1] (sorptivity, porosity accessible to water and initial moisture content) on the same samples used in [50].

First, capillary rise was simulated for the crack characteristics of the analysed problem using Eq. (24) as shown in Fig. 18. The equilibrium capillary rise was 51 mm, which was larger than the height of the crack and therefore complete saturation was used as boundary condition on the crack surfaces. The same boundary condition is applied at the plane $x = 0$ to simulate the capillary absorption experiment. The experiment was then simulated. In order to compare the horizontal moisture distribution, only the volume of the domain located between $x = 8$ mm and $x = 10$ mm is considered. This volume is further divided into small representative volumes (running along the z- axis) of dimensions $2 \times 0.4 \times 0.175$ mm (one such representative volume is shown in Fig. 17b). The saturation level and the z-coordinate of all Voronoi nodes located in a particular representative volume are averaged and plotted in order to compare the results with the experiments.

The results of the analysis, for a total time period of 60 min, considering the capillary suction in the crack are presented in Fig. 19. The experimental horizontal moisture profiles were available from unpublished data [51] available from the same experiment described in [50]. Fig. 19a shows the horizontal moisture distribution while Fig. 19b highlights a part of Fig. 19a to better show the moisture distribution

in the mortar matrix surrounding the crack. The penetration depth of the water around the crack for the different time stages obtained from the model are in close agreement with the experimental values. However, the horizontal moisture distribution curves for the different time stages have a somewhat different shape in the model compared to the experiments. The reason for this is that, in the simulations, the material is treated as homogeneous and the crack as planar of uniform width. In reality, non-porous inclusions (i.e. aggregates) are present in the material. In addition, the crack has not an ideal (i.e. parallel walled) shape constant crack width. Because of these approximations, the results in the numerical model show slight deviations from the experimental results.

4.3. Moisture transport in cracks of varying width

4.3.1. Experimental details

The experiment conducted in [52] is used as a reference to validate the model horizontal moisture distribution in cementitious materials with varying crack width. Prismatic specimens of dimensions $100 \times 100 \times 300$ mm cast with 6 steel bars of 8 mm diameter acting as reinforcements were studied in the experiments. A water–cement ratio of 0.6 and mortar mix-proportion of 1:3.3:0.6 (cement:sand:water) by volume was used. After curing for 14 days, the prisms were sliced along the long axis and smaller samples of size $25 \times 100 \times 300$ mm were obtained as shown in Fig. 20. The latter samples were subjected to three-point bending under controlled conditions to induce a single crack in the centre with maximum crack width of 0.35 mm. From the centre part of all the cracked specimens, slices of width 100 mm were cut as shown in Fig. 20 to obtain the samples of dimension $25 \times 100 \times 100$ mm with centred cracks. At the age of 28 days, these slices were dried for 4 days in a ventilated oven at 50° until constant weight was achieved.

All surfaces of the sample except the exposed (i.e. bottom) surface were sealed with self-adhesive aluminium foil to promote unidirectional moisture penetration. The specimen was then placed in a container and positioned in the path of the neutron beam. After the first radiograph on the dry sample, the container is filled with water so that only the bottom surface of the block is exposed, as shown in Fig. 20. Water starts penetrating into the crack and the surrounding porous matrix and the water distribution is monitored through neutron imaging at different time intervals. The diffusivity of the sound mortar was $D_0 = 1.54676 \times 10^{-4}$ mm^2/s, as determined by [52].

4.3.2. Numerical analysis

The cracked specimen used in the experiment was formed through three point bending and because of that the crack is wedge-shaped. In the numerical model, a triangular crack is implemented in the

---

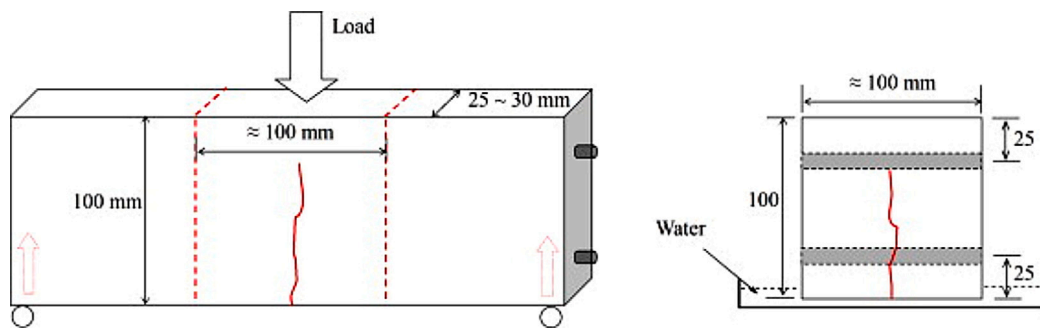[1] Raw data will be made available upon request.

Fig. 20. Formation of a centre crack under three point bending (left) and detached centre part in contact with water for observation of water penetration (right) [52].
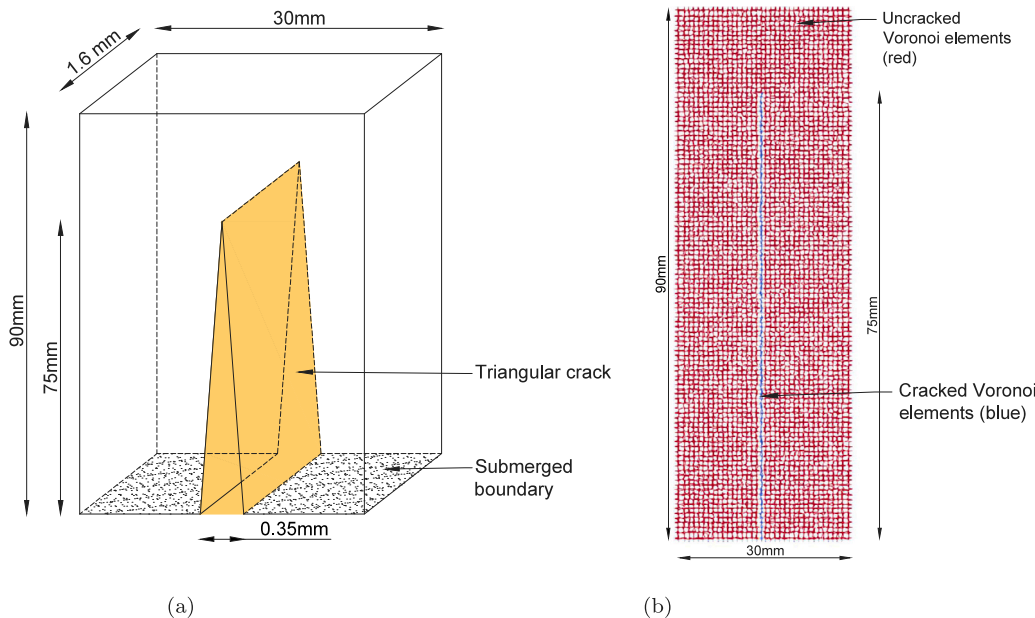

(a)

(b)

Fig. 21. Description of the numerical model, V shaped crack: (a) Voronoi mesh for transport, together with Delaunay elements in the crack; (b) geometry and boundary conditions.
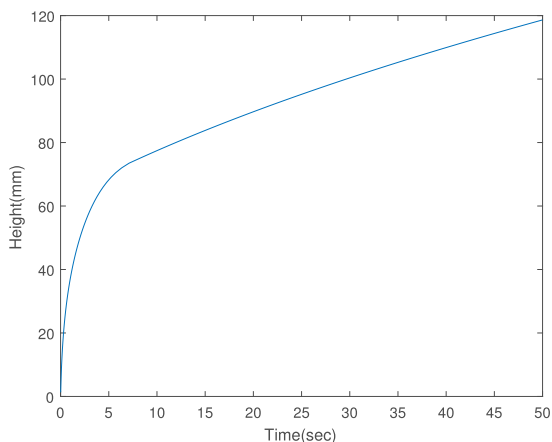

Fig. 22. Capillary rise in the V-shaped crack.

Table 5
Mesh Properties.

Parameter	Value
Number of nodes [-]	43536
Number of elements [-]	62214
Mean element length [mm]	0.4039
Crack width [mm]	0.35
Crack depth [mm]	75

domain surfaces are directly satisfied. The domain of dimensions $90 \times 1.6 \times 30$ mm^3 is generated with maximum crack width of 0.35 mm at the bottom and linearly decreasing width until a crack depth of 75 mm. The mesh properties of the discretized domain are given in Table 5 and the flow parameters used in the numerical model to simulate moisture transport are taken from precious given in Table 6. The later parameters were derived from a previous study performed by the same authors on the same material in [52], namely the previous study was published in [42].

The crack considered in this case does not have a uniform crack-width along its depth but varies linearly. For this case, the capillary suction in the crack is modelled using the discretized form of the modified Lucas–Washburn equation (Eq. (32)). The crack is divided into a number of discrete elements and the crack width for each discrete element is considered to be constant. Due to capillary suction, the crack becomes completely saturated in less than 10 s (see Fig. 22). As a result,

discretized domain in order to reproduce the nature of the crack used in the experiment as shown in Fig. 21b. The crack was generated using the Delaunay elements and the moisture transport in the crack and the surrounding elements is simulated through the Voronoi elements. The bottom surface is subjected to Dirichlet boundary condition of saturation level equal to 1, while the null flux across the rest of the

a) Exp 1 min   b) Sim 1 min   c) Exp 5 min   d) Sim 5 min

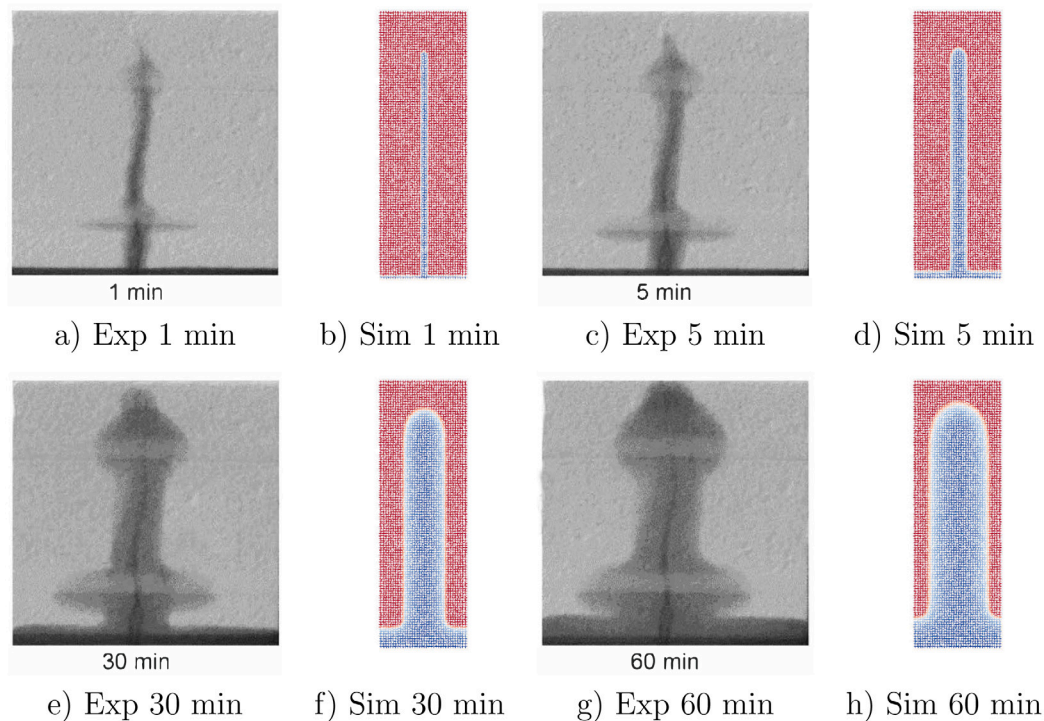e) Exp 30 min   f) Sim 30 min   g) Exp 60 min   h) Sim 60 min

Fig. 23. Comparison between experimental [45] (greyscale images) and numerical (colour images) moisture profiles of a cracked specimen subjected to capillary water absorption. (For interpretation of the references to colour in this figure legend, the reader is referred to the web version of this article.)

Table 6
Flow Parameters.

Parameter	Symbol	Value
Diffusivity of dry mortar [mm^2/s]	D_0	1.547×10^{-4}
Empirical constant [-]	n	6
Initial saturation [-]	θ_0	0
Porosity [-]	p	0.0462
Time step [s]	Δt	6

Fig. 24. Experimental and simulated horizontal moisture profiles for a crack of varying width.

by the time the moisture starts spreading into the surrounding concrete, the crack is already completely saturated and the crack faces act as additional submerged boundaries.

The experimental and numerical 2D moisture distribution of the studied sample is reported in Fig. 23 for the time stages of 1, 5, 30 and 60 min. It can be seen that the moisture profiles around the crack are similar to the ones obtained in the experiment. Note that the interface zone surrounding the reinforcement, which is known to present higher porosity and diffusivity [53], is not simulated, and therefore its influence cannot be observed in the numerical model. Furthermore, the activation of the reinforcement during loading may have altered the afore mentioned interface zone thus further modifying the diffusivity locally. Analogously, the influence of microcracking at the fracture process zone (at the tip) on the local transport properties of the concrete are also not modelled herein. The latter effect is evident in the experiments, as at the tip of the crack a small moisture profile bump can be more clearly observed at the radiograph acquired after 30 min of water absorption.

For quantitative comparison, the experimental and simulated horizontal moisture profiles (perpendicular to the crack) are also presented in Fig. 24. The profiled saturation from simulations was computed as an average for every distance from the crack in a sample height range from 20 to 50 mm. It can be noticed, that as in the case of water absorption in uncracked mortar presented in Section 3, at initial stages of the capillary absorption the simulated results seem to lag behind the experimental ones, while already at 30 and 60 min the compliance
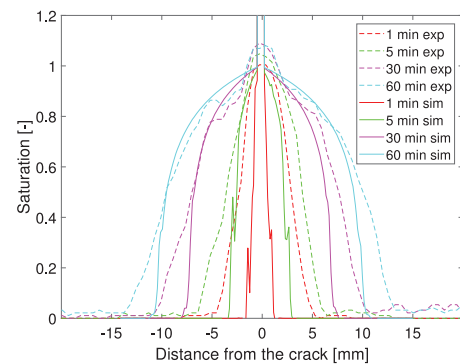
seems to improve dramatically. The latter similarity was not found in Section 4.2, where the imaging was carried out through X-ray micro Computed Tomography and therefore information along the depth of the sample was also available.

4.4. Moisture transport in deep cracks

In the examples studied in Sections 4.2 and 4.3 , the depth of the capillary water rise was sufficient to fill up the complete crack with water within seconds. Furthermore, the crack widths were small so the cracks could act as capillaries. In wider cracks, this might not be the case. In such a case capillary rise will be only limited to a fraction of the crack depth and the rest of the crack surface cannot be considered as an additional submerged boundary. The moisture transport in the remaining part of the crack is simulated by considering it a porous phase in mortar and the diffusivity is obtained through the cubic law (Eq. (32)). In this section, an example of a hypothetical crack in which the capillary water rise is not sufficient to fill up the crack is simulated.
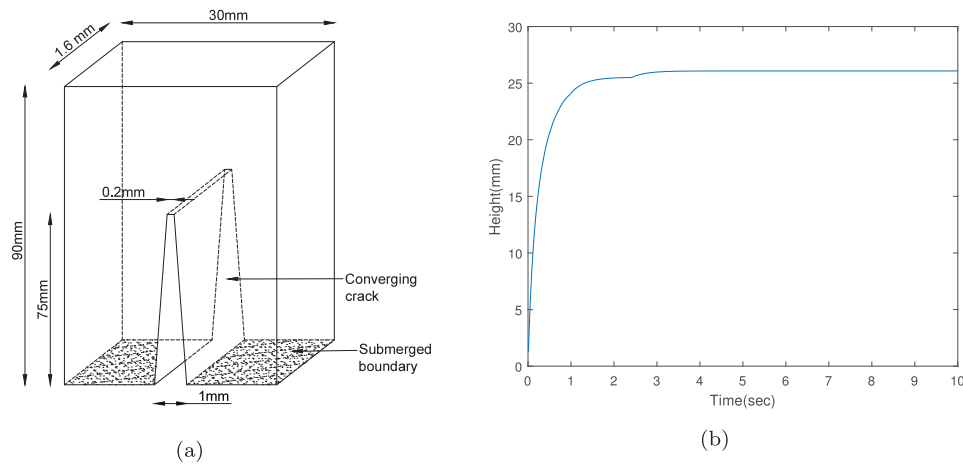
Fig. 25. Schematic of the sample and the trapezoidal crack.

The crack geometry as shown in Fig. 25a is used to simulate moisture transport. The crack width is decreasing from 1 mm to 0.2 mm over the crack depth, giving it a trapezoidal shape. The other parameters for the simulation are the same as given in Tables 5 and 6.

The crack is divided into discrete elements and the discretized form of the Lucas–Washburn equation gives the equilibrium height of the capillary rise as 26 mm shown in Fig. 25b. The crack surfaces until a depth of 26 mm will be completely submerged under capillary suction and act as additional submerged boundaries.

The horizontal and vertical moisture distribution of the crack are shown in Figs. 25 and 26, respectively. The crack is only partially saturated due to capillary suction and its effect is shown in the vertical moisture distribution for the initial time stages of 1 and 5 min (Fig. 26a, Fig. 26b). Until a crack depth of 26 mm, the water penetration into the surrounding matrix is uniform but for depths between 26 and 75 mm, the water penetration is higher where the crack width is wider and reduces as the crack width decreases, showing the dependence of the diffusivity of the crack on the crack width. Once the crack becomes saturated, the penetration of water from the crack to the adjoining matrix is uniform. The horizontal moisture distribution and the vertical moisture distribution for the later time stages is similar to the ones obtained in the numerical models used to simulate the experiments.

The rates and magnitudes of the capillary rise computed using the modified Lucas–Washburn equation proposed in [49] Figs. 18, 22 and 25(b) for parallel-walled, narrow-wedged and wide-wedged cracks, respectively) present marked differences. Namely, for similar crack mouth openings 0.35 and 0.37 mm (Figs. 18 and 22) the equilibrium height of the capillary rise results notably higher for wedged crack, when compared to parallel-walled crack. In the model this is due to the decreasing crack width in the wedge crack for which capillarity forces overcome the gravitational effects beyond 50 mm (the capillary rise of the parallel-walled crack). Furthermore, it could be observed that the height vs. time curve does not reach a plateau in the case of the wedged crack as the radius of the capillary tends to zero towards the fracture process zone. For the hypothetical wedged crack reported in Figs. 25(b), with a crack mouth width of 1 mm, the capillary equilibrium height is found to be inferior to that of the narrower wedged crack in Figs. 22. In the model, this is again due to the lower counteraction to gravity by the capillary forces which are lower because inversely proportional to the "capillary radius".

5. Conclusions

In this work, various numerical aspects of using a dual-lattice approach for simulating capillary moisture flow in sound and cracked concrete are presented. The influence of different possible approximations, commonly used to reduce computational time, on the accuracy of the obtained simulation results are discussed in detail. Furthermore, an approach for simulating of capillary moisture uptake in cracked cementitious materials is presented and discussed. Based on the obtained results, the following can be concluded:

- When the diffusivity is constant, the transport model based on the Voronoi discretization of the domain is able to simulate both the steady-state and the non-steady state diffusion process, and shows an excellent comparison with the analytical solutions of benchmark cases. No spurious oscillations were observed in the numerical model as a result of the mesh randomness.
- The transport model based on the Voronoi discretization is able to reproduce the experimental capillary moisture ingress in sound mortar. Some deviation between the numerical and the experimental results appears at later stages of the process. A cause for such discrepancies could be attributed to additional physical phenomena not included in the model such as: (i) non-uniform distribution of flow parameters due to heterogeneities in the concrete, (ii) longer-term flow anomalies due to the effect of capillary imbibition [47] and/or gravity [46].
- Approximations commonly used in (dual) lattice models when simulating moisture flow, such as the simplified calculation of the elemental diffusivity and volumetric capacity and the explicit time stepping scheme resulted in enough accuracy of the numerical solution for the studied problems. This sufficient accuracy was achieved by selecting appropriately small time steps and mesh sizes.
- Capillary moisture uptake in cracks can successfully be simulated by considering two phenomena: (i) capillary uptake in the exposed part of the crack until the equilibrium height is achieved, and (ii) increased moisture diffusion in the part of the crack which is above this equilibrium height. The occurrence and predominance of these two mechanisms depends on the geometry of the crack, i.e. the height and the width. The obtained results show good correspondence with experimental data.

In this work, most of the simulations and their analyses are carried out for relatively short time frames up to 8 h of moisture absorption. Whereas short moisture exposures are characteristic in concrete structures exposed to wet and dry cycles, longer exposures to rain or partial submersion are not extremely rare. Therefore, in the future further investigations of the numerical framework presented herein for longer times need to be performed to maximize its applicability to a vast array of exposure conditions.
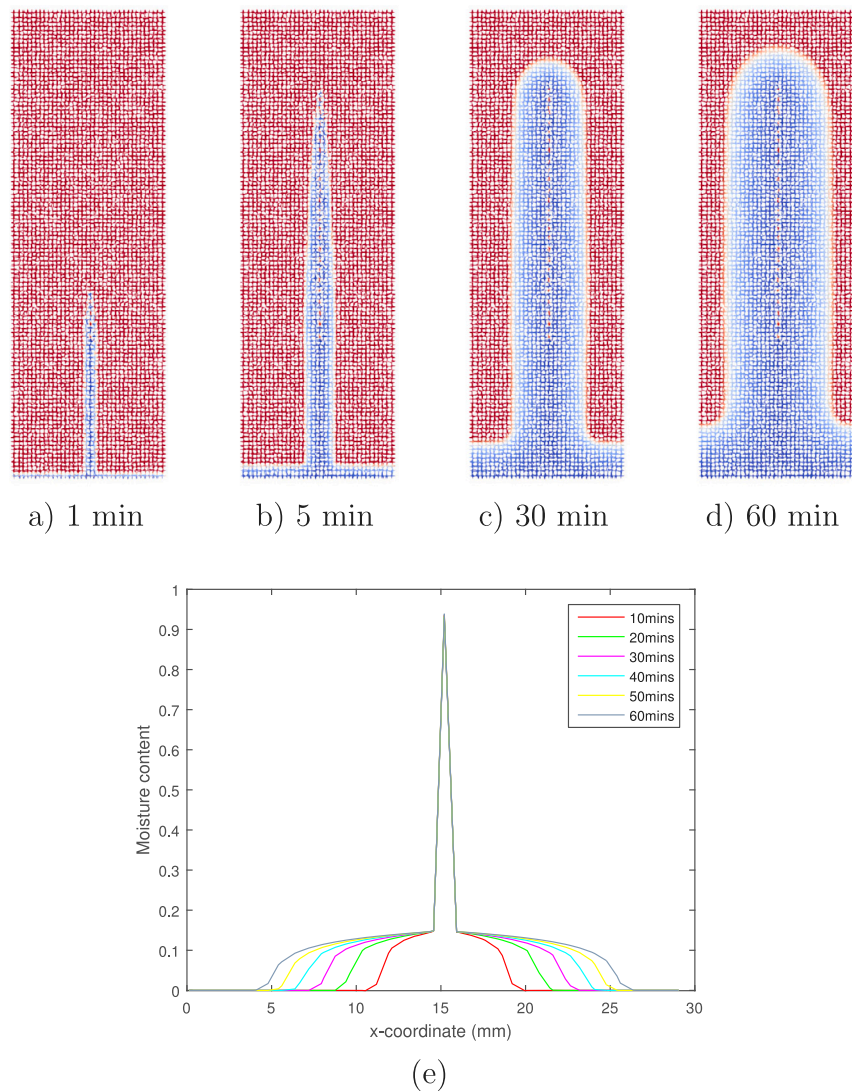
Fig. 26. Vertical moisture distribution in the trapezoidal crack after (a) 1 min, (b) 5 min, (c) 30 min and (d) 60 min and horizontal moisture distribution in the trapezoidal crack (e).

CRediT authorship contribution statement

Anmol Singla: Conceptualization, Methodology, Software, Formal analysis, Investigation, Writing – original draft, Visualization. **Branko Šavija:** Conceptualization, Methodology, Software, Methodology, Writing – original draft, Writing – review & editing, Supervision. **Lambertus J. Sluys:** Resources, Writing – review & editing, Supervision, Funding acquisition. **C. Romero Rodríguez:** Conceptualization, Software, Methodology, Software, Writing – original draft, Writing – review & editing, Supervision.

Declaration of competing interest

The authors declare that they have no known competing financial interests or personal relationships that could have appeared to influence the work reported in this paper.

Acknowledgements

References

[1] P.K. Mehta, P.J. Monteiro, Concrete microstructure, properties and materials, 2017.
[2] B. Šavija, E. Schlangen, J. Pacheco, S. Millar, T. Eichler, G. Wilsch, Chloride ingress in cracked concrete: a laser induced breakdown spectroscopy (LIBS) study, J. Adv. Concr. Technol. 12 (10) (2014) 425–442.
[3] B. Šavija, M. Luković, E. Schlangen, Influence of cracking on moisture uptake in strain-hardening cementitious composites, J. Nanomech. Micromech. 7 (1) (2017) 04016010.
[4] P. Grassl, H.S. Wong, N.R. Buenfeld, Influence of aggregate size and volume fraction on shrinkage induced micro-cracking of concrete and mortar, Cem. Concr. Res. 40 (1) (2010) 85–93.
[5] H. Wong, M. Zobel, N. Buenfeld, R. Zimmerman, Influence of the interfacial transition zone and microcracking on the diffusivity, permeability and sorptivity of cement-based materials after drying, Mag. Concr. Res. 61 (8) (2009) 571–589.
[6] A. Blagojević, The Influence of Cracks on the Durability and Service Life of Reinforced Concrete Structures in Relation to Chloride-Induced Corrosion (Ph.D. thesis), Delft University of Technology, Netherlands, 2016.
[7] Z. Pan, R. Ma, D. Wang, A. Chen, A review of lattice type model in fracture mechanics: theory, applications, and perspectives, Eng. Fract. Mech. 190 (2018) 382–409.
[8] M. Nikolić, E. Karavelić, A. Ibrahimbegovic, P. Miščević, Lattice element models and their peculiarities, Arch. Comput. Methods Eng. 25 (3) (2018) 753–784.
[9] E. Schlangen, E. Garboczi, Fracture simulations of concrete using lattice models: computational aspects, Eng. Fract. Mech. 57 (2–3) (1997) 319–332.
[10] J. Bolander Jr., S. Saito, Fracture analyses using spring networks with random geometry, Eng. Fract. Mech. 61 (5–6) (1998) 569–591.

[11] H. Zhang, B. Šavija, S.C. Figueiredo, E. Schlangen, Experimentally validated multi-scale modelling scheme of deformation and fracture of cement paste, Cem. Concr. Res. 102 (2017) 175–186.

[12] C.R. Rodríguez, F.F. de Mendonça Filho, L. Mercuri, Y. Gan, E. Rossi, G. Anglani, P. Antonaci, E. Schlangen, B. Šavija, Chemo-physico-mechanical properties of the interface zone between bacterial PLA self-healing capsules and cement paste, Cem. Concr. Res. 138 (2020) 106228.

[13] H. Zhang, Y. Xu, Y. Gan, E. Schlangen, B. Šavija, Experimentally validated meso-scale fracture modelling of mortar using output from micromechanical models, Cem. Concr. Compos. 110 (2020) 103567.

[14] B.B. Aydin, K. Tuncay, B. Binici, Simulation of reinforced concrete member response using lattice model, J. Struct. Eng. 145 (9) (2019) 04019091.

[15] J.E. Bolander, S. Choi, S.R. Duddukuri, Fracture of fiber-reinforced cement composites: effects of fiber dispersion, Int. J. Fract. 154 (1–2) (2008) 73–86.

[16] B. Šavija, J.a. Feiteira, M. Araújo, S. Chatrabhuti, J.-M. Raquez, K. Van Tittelboom, E. Gruyaert, N. De Belie, E. Schlangen, Simulation-aided design of tubular polymeric capsules for self-healing concrete, Materials 10 (1) (2017) 10.

[17] L.-Y. Lv, H. Zhang, E. Schlangen, Z. Yang, F. Xing, Experimental and numerical study of crack behaviour for capsule-based self-healing cementitious materials, Constr. Build. Mater. 156 (2017) 219–229.

[18] Z. Chang, H. Zhang, E. Schlangen, B. Šavija, Lattice fracture model for concrete fracture revisited: Calibration and validation, Appl. Sci. 10 (14) (2020) 4822.

[19] E. Schlangen, J. Van Mier, Simple lattice model for numerical simulation of fracture of concrete materials and structures, Mater. Struct. 25 (9) (1992) 534–542.

[20] J.E. Bolande Jr., S. Berton, Simulation of shrinkage induced cracking in cement composite overlays, Cem. Concr. Compos. 26 (7) (2004) 861–871.

[21] P. Grassl, A lattice approach to model flow in cracked concrete, Cem. Concr. Compos. 31 (7) (2009) 454–460.

[22] B. Šavija, J. Pacheco, E. Schlangen, Lattice modeling of chloride diffusion in sound and cracked concrete, Cem. Concr. Compos. 42 (2013) 30–40.

[23] L. Wang, J. Bao, T. Ueda, Prediction of mass transport in cracked-unsaturated concrete by mesoscale lattice model, Ocean Eng. 127 (2016) 144–157.

[24] B. Šavija, M. Luković, E. Schlangen, Lattice modeling of rapid chloride migration in concrete, Cem. Concr. Res. 61 (2014) 49–63.

[25] Z. Pan, A. Chen, R. Ma, D. Wang, H. Tian, Three-dimensional lattice modeling of concrete carbonation at meso-scale based on reconstructed coarse aggregates, Constr. Build. Mater. 192 (2018) 253–271.

[26] L. Liu, X. Wang, H. Chen, C. Wan, M. Zhang, Numerical modeling of drying shrinkage deformation of cement-based composites by coupling multiscale structure model with 3D lattice analyses, Comput. Struct. 178 (2017) 88–104.

[27] M. Luković, B. Šavija, E. Schlangen, G. Ye, K. Van Breugel, A 3D lattice modelling study of drying shrinkage damage in concrete repair systems, Materials 9 (7) (2016) 575.

[28] P. Grassl, C. Fahy, D. Gallipoli, S.J. Wheeler, On a 2D hydro-mechanical lattice approach for modelling hydraulic fracture, J. Mech. Phys. Solids 75 (2015) 104–118.

[29] M. Nikolic, A. Ibrahimbegovic, P. Miscevic, Discrete element model for the analysis of fluid-saturated fractured poro-plastic medium based on sharp crack representation with embedded strong discontinuities, Comput. Methods Appl. Mech. Engrg. 298 (2016) 407–427.

[30] H. Nakamura, W. Srisoros, R. Yashiro, M. Kunieda, Time-dependent structural analysis considering mass transfer to evaluate deterioration process of RC structures, J. Adv. Concr. Technol. 4 (1) (2006) 147–158.

[31] P. Grassl, J. Bolander, Three-dimensional network model for coupling of fracture and mass transport in quasi-brittle geomaterials, Materials 9 (9) (2016) 782.

[32] A. Fascetti, C. Oskay, Dual random lattice modeling of backward erosion piping, Comput. Geotech. 105 (2019) 265–276.

[33] T. Saka, Simulation of Reinforced Concrete Durability: Dual-Lattice Models of Crack-Assisted Mass Transport (Ph.D. thesis), University of California, Davis, USA, 2012.

[34] C.R. Rodríguez, S.C. Figueiredo, E. Schlangen, D. Snoeck, Modeling water absorption in cement-based composites with sap additions, in: Computational Modelling of Concrete Structures, CRC Press, 2018, pp. 295–304.

[35] M. Yip, J. Mohle, J. Bolander, Automated modeling of three-dimensional structural components using irregular lattices, Comput.-Aided Civ. Infrastruct. Eng. 20 (6) (2005) 393–407.

[36] L.A. Richards, Capillary conduction of liquids through porous mediums, Physics 1 (5) (1931) 318–333.

[37] C. Hall, Water sorptivity of mortars and concretes: a review, Mag. Concr. Res. 41 (147) (1989) 51–61.

[38] D. Lockington, J.-Y. Parlange, P. Dux, Sorptivity and the estimation of water penetration into unsaturated concrete, Materials and Structures 32 (5) (1999) 342.

[39] C.R. Rodríguez, S.C. Figueiredo, M. Deprez, D. Snoeck, E. Schlangen, B. Šavija, Numerical investigation of crack self-sealing in cement-based composites with superabsorbent polymers, Cem. Concr. Compos. 104 (2019) 103395.

[40] C. Hall, W.D. Hoff, Water Transport in Brick, Stone and Concrete, CRC Press, 2011.

[41] R.W. Lewis, P. Nithiarasu, K.N. Seetharamu, Fundamentals of the Finite Element Method for Heat and Fluid Flow, John Wiley & Sons, 2004.

[42] P. Zhang, T.-J. Zhao, F. Wittmann, E. Lehmann, Water capillary suction dynamics of cement-based materials based on neutron radiography method, Shuili Xuebao(J. Hydraul. Eng.) 42 (1) (2011) 81–87.

[43] L.-C. Wang, Analytical relationship between capillarity coefficient and sorptivity of building material, J. Hydraul. Eng. 40 (2009) 1085–1090.

[44] L. Hanžič, R. Ilić, Relationship between liquid sorptivity and capillarity in concrete, Cem. Concr. Res. 33 (9) (2003) 1385–1388.

[45] P. Zhang, F.H. Wittmann, T.-j. Zhao, E.H. Lehmann, P. Vontobel, Neutron radiography, a powerful method to determine time-dependent moisture distributions in concrete, Nucl. Eng. Des. 241 (12) (2011) 4758–4766.

[46] C. Hall, Anomalous diffusion in unsaturated flow: Fact or fiction? Cem. Concr. Res. 37 (3) (2007) 378–385, http://dx.doi.org/10.1016/j.cemconres.2006.10.004, URL: http://linkinghub.elsevier.com/retrieve/pii/S000888460600250X.

[47] N.M. Alderete, Y.V. Zaccardi, N. De Belie, Physical evidence of swelling as the cause of anomalous capillary water uptake by cementitious materials, Cem. Concr. Res. 120 (2019) 256–266.

[48] G.L. Sleijpen, H.A. Van der Vorst, D.R. Fokkema, BiCGstab (l) and other hybrid Bi-CG methods, Numer. Algorithms 7 (1) (1994) 75–109.

[49] D. Gardner, A. Jefferson, A. Hoffman, Investigation of capillary flow in discrete cracks in cementitious materials, Cem. Concr. Res. 42 (7) (2012) 972–981.

[50] C. Romero Rodriguez, M. Deprez, F. França de Mendonça Filho, S. van Offenwert, V. Cnudde, H. Schlangen, B. Šavija, X-Ray micro tomography of water absorption by superabsorbent polymers in mortar, in: RILEM Bookseries, vol. 24, Springer, 2020.

[51] C. Romero Rodriguez, Time-resolved differential micro CT to monitor unsaturated water transport in cement-based materials, 2018, In preparation for submission to Materials.

[52] P. Zhang, F. Wittmann, T. Zhao, E. Lehmann, Neutron imaging of water penetration into cracked steel reinforced concrete, Physica B 405 (7) (2010) 1866–1871.

[53] Y. Goto, K. Otsuka, Experimental studies on cracks formed in concrete around deformed tension bars, in: Proceedings of the Japan Society of Civil Engineers, Vol. 1980, no. 294, Japan Society of Civil Engineers, 1980, pp. 85–100.